I&EC research
Industrial & Engineering Chemistry Research

pubs.acs.org/IECR

Article

Modeling the Local Environment within Porous Electrode during Electrochemical Reduction of Bicarbonate

Recep Kas, Kailun Yang, Gaurav P. Yewale, Allison Crow, Thomas Burdyny, and Wilson A. Smith*

Cite This: *Ind. Eng. Chem. Res.* 2022, 61, 10461−10473

Read Online

ACCESS | Metrics & More | Article Recommendations | Supporting Information

ABSTRACT: The electrochemical reduction of bicarbonate to renewable chemicals without external gaseous CO_2 supply has been motivated as a means of integrating conversion with upstream CO_2 capture. The way that CO_2 is formed and transported during CO_2-mediated bicarbonate reduction in flow cells is profoundly different from conventional CO_2 saturated and gas-fed systems and a thorough understanding of the process would allow further advancements. Here, we report a comprehensive two-phase mass transport model to estimate the local concentration of species in the porous electrode resultant from homogeneous and electrochemical reactions of (bi)carbonate and CO_2. The model indicates that significant CO_2 is generated in the porous electrode during electrochemical reduction, even though the starting bicarbonate solution contains negligible CO_2. However, the in situ formation of CO_2 and subsequent reduction to CO exhibits a plateau at high potentials due to neutralization of the protons by the alkaline reaction products, acting as the limiting step toward higher CO current densities. Nevertheless, the pH in the catalyst layer exhibits a relatively smaller rise, compared to conventional electrochemical CO_2 reduction cells, because of the reaction between protons and CO_3^{2-} and OH^- that is confined to a relatively small volume. A large fraction of the CL exhibits a mildly alkaline environment at high current densities, while an appreciable amount of carbonic acid (0.1−1 mM) and a lower pH exist adjacent to the membrane, which locally favor hydrogen evolution, especially at low electrolyte concentrations. The results presented here provide insights into local cathodic conditions for both bicarbonate cells and direct-CO_2 reduction membrane electrode assembly cells utilizing cation exchange membranes facing the cathode.

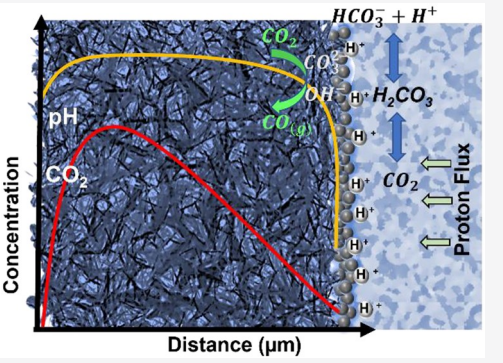

INTRODUCTION

The electrochemical reduction of CO_2 to fuels and precursor chemicals has been heavily investigated over the past decade as a potential solution to mitigate CO_2 emissions while storing renewable electricity in chemical bonds.[1,2] Standard electrochemical cells utilize purified gaseous CO_2 as the primary feedstock for the electrochemical reduction of CO_2 to CO, formate, and multicarbon products.[3] To obtain purified high-pressure CO_2, CO_2 must be captured from point sources or directly from the atmosphere, regenerated, and pressurized.[4] The direct electrochemical reduction of CO_2 from carbon capture solutions might enable bypassing the energy and capital-intensive regeneration and compression steps.[5−7] Direct electrolysis of capture solutions may be also beneficial for separation costs and complexity when the products are gaseous.

The most mature technology for CO_2 capture and purification utilizes primary amines.[8] There have been two commercial-scale power plants (one still operating) utilizing amine-based capture technology.[9] Direct electrochemical reduction of CO_2 to CO from aqueous amine solutions has been reported recently to utilize CO_2 as a building block for commodity chemicals.[10] An alternative capture technology has been proposed to lower the cost and increase the efficiency of the carbon capture process which is based on the reaction of CO_2 and hydroxide ions in ammonium and alkali hydroxide solutions.[4,11] The resultant capture solutions contain (bi)-carbonates which can be reduced to valuable chemicals without the need for regeneration of gaseous CO_2.[6,12,13]

The first investigations of electrochemical conversion of bicarbonate were reported by Hori et al. where formate was produced on mercury electrodes in argon-saturated 1 M $NaHCO_3$ solutions.[14] Furthermore, studies of bicarbonate reduction to formate were reported in standard electrochemical cells on Cu, Pd, and Sn electrodes where the partial current densities were typically low (<5 mA/cm^2).[15−17] In these studies, reduction of bicarbonate was proposed to occur via in situ formation of CO_2 near the electrode surface or reactions with the adsorbed hydrogen on metal electrodes. More recently, membrane electrode assembly (MEA)-type

Special Issue: Engineered Methodologies for CO2 Utilization

Received: January 27, 2022
Revised: April 6, 2022
Accepted: April 7, 2022
Published: April 22, 2022

flow cells equipped with a bipolar membrane (BPM) or a cation exchange membrane (CEM) have been reported for bicarbonate reduction.[5,6] These systems locally produce CO_2 from the reaction between (bi)carbonate ions and protons conducted via the membrane, providing a local source of CO_2 for conversion to CO. The maximum partial current density of CO (~40 mA cm^{-2}) in these bicarbonate flow cells is comparable to the ones in CO_2 saturated aqueous solutions, while the reported Faradaic efficiencies (FE) of CO is typically lower (<50%).[5] With further experimental investigations into the structure of the porous diffusion media and catalyst layer, however, Lees et al. achieved performances exceeding 100 mA cm^{-2} yet still with a moderate CO selectivity (<60%).[18] These increases indicate that there is room for improvement in the performance metrics of bicarbonate reduction if the underlying chemical reactions and transport phenomena through the catalyst layer were better understood.

The experimental studies in bicarbonate flow cells suggested that a proton conductive membrane is required to be adjacent to the catalyst layer to achieve reasonable current densities and the reduction takes place via locally produced CO_2.[5,18] When anion exchange membranes are used, local generation of CO_2 occurs at the anode/membrane interface which leads to lower CO_2 utilization and selectivity.[19,20] The studies in MEA type of gas-fed systems utilizing a BPM then attributed increased the hydrogen evolution reaction (HER) at high current densities to be due to a high proton flux and an acidic environment in the catalyst layer(CL) that then hurt CO selectivity.[21] On the contrary, in situ Raman spectroscopy studies on the opposite side of the electrode, i.e., flow channel-electrode interface, suggested the existence of an local alkaline environment.[22] Combined, these hypotheses indicate a high local variation of the involved carbon species as a result of the numerous competing electrochemical and homogeneous reactions in the system. As the operational window for selective CO production via bicarbonate electrolysis is narrow, it is essential that the local variations across the system are understood and intentionally designed. However, the number of studies in bicarbonate electrolysis is relatively small, and modeling efforts in bicarbonate electrolysis have yet to performed.

Despite the absence of mass transport models for bicarbonate electrolysis, models have been extensively used to correlate the local concentrations of species to the activity and selectivity of the catalysts in CO_2 saturated aqueous solutions.[23,24] Recently, mass transport models for gas-fed systems were developed with a flowing catholyte and MEA type of configuration using anion exchange membranes-(AEM).[25−28] However, the local conditions in bicarbonate flow cells can be profoundly different from the gas-fed systems and CO_2 saturated aqueous solutions, because of the differences in CO_2 and proton supply to the electrode.

In this study, we report a two-phase one-dimensional (1-D) mass transport model for the cathode of the bicarbonate flow cell to quantify the local concentration of the species in the porous diffusion media (DM) and CL under varying operating conditions. We compared the performance of the electrochemical model with experimental studies in the literature by determining the variation of the current densities and FE with different applied potentials. Our model suggests that the formation of CO is purely limited by mass transport and/or the formation of CO_2 starting from very low current densities (>25 mA cm^{-2}), compared to being limited by HER. The partial current density of CO then exhibits a plateau when protons conducted from the membrane are balanced out by electrochemically produced CO_3^{2-} and OH^-. Simultaneously, the pH adjacent to the membrane drops and appreciable amounts of carbonic acid are produced in the CL, which locally favors hydrogen evolution, particularly at low electrolyte concentrations. We believe the modeling results can be helpful to understand the limiting factors of bicarbonate flow cells and provide insights for further enhancing the activity and selectivity by using chemical and engineering approaches.

MODEL DESCRIPTION

A 1-D model of the cathode of a bicarbonate flow cell including a porous DM and Ag porous CL was modeled at steady state and under isothermal conditions. A schematic representation of the two-phase model with associated boundary conditions and chemical reactions is given in Figure 1. The bicarbonate flow cell was operated at ambient

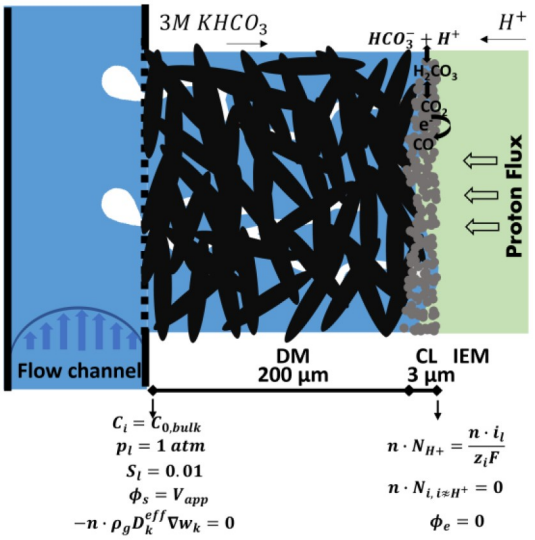

Figure 1. Schematic illustration of the 1-D model including the boundary conditions. Here, bicarbonate is provided as a primary reactant from the flow channel and diffuses through the diffusion media to the catalyst layer, where additional reactions occur.

temperature, which was fixed at 298.15 K. The diffusion medium properties have been adapted from carbon papers. These do not contain additional polytetrafluoroethylene (PTFE) treatment or a microporous layer (see Table 1). These porous media are commonly used as a gas diffusion electrode (GDE) after treatment with PTFE and the addition of a microporous layer. Since the bicarbonate electrolysis utilizes liquid electrolytes, we referred to these structures as DM in this paper. The cation exchange membrane pressed against the catalyst layer and the flow channel supplying the liquid electrolyte and removing the gas bubbles were included as interfaces.

Both the DM and CL were initially flooded with a 3 M potassium bicarbonate ($KHCO_3$) solution that was not saturated by CO_2 and contained dissolved ions including CO_2, H^+, K^+, OH^-, HCO_3^-, H_2CO_3, and CO_3^{2-}. The concentrations of the CO_2, (bi)carbonate species, and pH of the solution are driven by the following homogeneous reactions:

https://doi.org/10.1021/acs.iecr.2c00352
Ind. Eng. Chem. Res. 2022, 61, 10461−10473

Table 1. List of Parameters

parameter	value	units	ref
$D_{HCO_3^-}$	1.19×10^{-9}	$m^2\ s^{-1}$	39
$D_{CO_3^{2-}}$	9.23×10^{-10}	$m^2\ s^{-1}$	39
D_{OH^-}	5.29×10^{-9}	$m^2\ s^{-1}$	39
D_{H^+}	9.31×10^{-9}	$m^2\ s^{-1}$	39
D_{CO_2}	1.91×10^{-9}	$m^2\ s^{-1}$	39
D_{K^+}	1.96×10^{-9}	$m^2\ s^{-1}$	39
$D_{H_2CO_3}$	1.81×10^{-9}	$m^2\ s^{-1}$	40
$E^o_{H_2}$	0.0	V	2
E^o_{CO}	−0.11	V	41
i^0_{CO,H_2O}	3.4×10^{-4}	$A\ m^{-2}$	42
i^0_{CO,HCO_3^-}	6×10^{-3}	$A\ m^{-2}$	
$i^0_{H_2,H_2O}$	3.3×10^{-6}	$A\ m^{-2}$	43
$i^0_{H_2,HCO_3^-}$	5.8×10^{-5}	$A\ m^{-2}$	
$i^0_{H_2,acid}$	3×10^{-3}	$A\ m^{-2}$	44
k_1^f	6.5×10^{7}	$m^3\ s^{-1}\ mol^{-1}$	29
k_1^b	1.1×10^{7}	s^{-1}	29
k_2^f	2.86×10^{1}	s^{-1}	45, 46
k_2^b	7×10^{-2}	s^{-1}	45, 46
k_3^f	9.98	s^{-1}	45
k_3^b	5×10^{7}	$m^3\ s^{-1}\ mol^{-1}$	45
k_4^f	6×10^{6}	$m^3\ s^{-1}\ mol^{-1}$	45
k_4^b	3×10^{5}	s^{-1}	45
k_5^f	2.23	$m^3\ s^{-1}\ mol^{-1}$	45
k_5^b	5.35×10^{-5}	s^{-1}	45
k_6^f	2.29×10^{-1}	$mol\ m^{-3}\ s^{-1}$	45, 47
k_6^b	2.31×10^{7}	$m^3\ s^{-1}\ mol^{-1}$	45, 47
k_7^f	1×10^{7}	$m^3\ s^{-1}\ mol^{-1}$	29
k_7^b	5.9×10^{-1}	s^{-1}	29
k_8^f	2.04×10^{-2}	$m^3\ s^{-1}\ mol^{-1}$	29
k_8^b	5×10^{-5}	$m^3\ s^{-1}\ mol^{-1}$	29
k_9^f	1.14×10^{-1}	$m^3\ s^{-1}\ mol^{-1}$	48
k_9^b	5.49×10^{-5}	$m^3\ s^{-1}\ mol^{-1}$	48
k_{10}^f	1.4×10^{-1}	$m^6\ s^{-1}\ mol^{-2}$	29
k_{10}^b	3×10^{-6}	$m^3\ s^{-1}\ mol^{-1}$	29
k_{mt}	1×10^{2}	s^{-1}	49
I_{vg}	0.5		50
m_{vg}	0.86		51
a_v	1×10^{7}	m^{-1}	27
α_{CO}	0.33		52
α_{H_2}	0.3		53
$\alpha_{H_2,acid}$	0.36		27
ε_{dm}	0.8		54
ε_{cl}	0.7		27
κ_{dm}	1×10^{-11}	m^2	54
κ_{cl}	1×10^{-15}	m^2	55
ρ_l	1175	$kg\ m^{-3}$	56
σ_{dm}	220	$S\ m^{-1}$	27
σ_{cl}	100	$S\ m^{-1}$	27
μ_l	1.8×10^{-3}	Pa s	57
μ_g	1.33×10^{-5}	Pa s	56

$$H^+ + HCO_3^- \underset{k_1^b}{\overset{k_1^f}{\rightleftharpoons}} H_2CO_3 \quad (1)$$

$$H_2CO_3 \underset{k_2^b}{\overset{k_2^f}{\rightleftharpoons}} CO_2 + H_2O \quad (2)$$

$$HCO_3^- \underset{k_3^b}{\overset{k_3^f}{\rightleftharpoons}} H^+ + CO_3^{2-} \quad (3)$$

$$HCO_3^- + OH^- \underset{k_4^b}{\overset{k_4^f}{\rightleftharpoons}} CO_3^{2-} + H_2O \quad (4)$$

$$CO_2 + OH^- \underset{k_5^b}{\overset{k_5^f}{\rightleftharpoons}} HCO_3^- \quad (5)$$

$$H_2O \underset{k_6^b}{\overset{k_6^f}{\rightleftharpoons}} H^+ + OH^- \quad (6)$$

$$H_2CO_3 + OH^- \underset{k_7^b}{\overset{k_7^f}{\rightleftharpoons}} HCO_3^- + H_2O \quad (7)$$

In-situ spectroscopic and isotope labeling studies have also suggested that additional reactions exist in high concentrations of (bi)carbonate (>0.5M),[29,30]

$$CO_2 + HCO_3^- + H_2O \underset{k_8^b}{\overset{k_8^f}{\rightleftharpoons}} H_2CO_3 + HCO_3^- \quad (8)$$

$$CO_2 + CO_3^{2-} + H_2O \underset{k_9^b}{\overset{k_9^f}{\rightleftharpoons}} 2HCO_3^- \quad (9)$$

$$CO_2 + OH^- + CO_3^{2-} \underset{k_{10}^b}{\overset{k_{10}^f}{\rightleftharpoons}} CO_3^{2-} + HCO_3^- \quad (10)$$

The electrochemical reduction of aqueous CO_2 to CO at the electrode surface occurs with the addition of electrons and a proton source. Within the operating parameters considered here, there are four possible proton sources for the electrochemical reactions. These are bicarbonate, water, hydronium ions, and carbonic acid (see eqs 11−14). HCO_3^- can act as a major proton donor at high concentrations (>0.2 M) via the reaction[31,32]

$$CO_2 + 2HCO_3^- + 2e^- \rightleftharpoons CO_{(g)} + 2CO_3^{2-} \quad (11)$$

Water can act as a proton donor when high enough potentials are applied via

$$CO_2 + H_2O + 2e^- \rightleftharpoons CO_{(g)} + 2OH^- \quad (12)$$

and under acidic conditions, the protons from hydronium ion and carbonic acid can act as proton donors and the following reactions can be written for CO_2 reduction:

$$CO_2 + 2H_3O^+ + 2e^- \rightleftharpoons CO_{(g)} + 2H_2O \quad (13)$$

$$CO_2 + 2H_2CO_3 + 2e^- \rightleftharpoons CO_{(g)} + 2HCO_3^- + H_2O \quad (14)$$

CO_2 reduction via high hydronium ion and carbonic acid as proton donors were assumed to be negligible and HER was assumed to dominate under acidic conditions. In concentrated bicarbonate solutions, alkaline and acidic conditions, HER can occur via the following reactions:

$$2HCO_3^- + 2e^- \rightleftharpoons H_2 + 2CO_3^{2-} \quad (15)$$

$$2H_2O + 2e^- \rightleftharpoons H_2 + 2OH^- \quad (16)$$

$$2H_3O^+ + 2e^- \rightleftharpoons H_2 + 2H_2O \quad (17)$$

$$2H_2CO_3 + 2e^- \rightleftharpoons H_2 + 2HCO_3^- \quad (18)$$

https://doi.org/10.1021/acs.iecr.2c00352
Ind. Eng. Chem. Res. 2022, 61, 10461−10473

Here, HER from the hydronium ion (eq 17) and carbonic acid (eq 18) were assumed to occur with the same kinetic parameters (see Table 1). However, there might be slight differences in kinetic parameters, as a result of differences in pK_a, which has not been reported, to the best of our knowledge.

Rates of Homogeneous and Electrode Reactions. For homogeneous reactions in the bulk electrolyte, none of the reactions were assumed to be in equilibrium and kinetic expressions were used to calculate the rate of reaction i ($R_{B,i}$) via

$$R_{B,i} = \nu_i \left(k_i^f \prod_{i=\text{react}} c_i^{\nu_i} - k_i^b \prod_{i=\text{prod}} c_i^{\nu_i} \right) \tag{19}$$

where c_i is the concentration of species i. The stoichiometric coefficient is denoted by ν_i and forward and backward rate constants are donated by k_i^f and k_i^b, respectively. The equilibrium constant (K_{eq}^i) is given by $K_{eq}^i = k_i^f/k_i^b$. K_{eq}^i was used to calculate the forward or backward rate constants after correction for ionic strength. The electrochemical reactions were assumed to follow concentration-dependent Volmer-Butler kinetics:

$$i_m = -i_{0,m} \left(\frac{c_i}{c_i^{ref}} \right)^{\delta_i} e^{-\frac{\alpha_m F \eta_m}{RT}} \tag{20}$$

where i_m, i_m^0, α_m, and η_m is the partial current density, exchange current density, cathodic transfer coefficient, and overpotential of reaction m, respectively. c_i and δ_i denote the concentration of species i, and order of the reaction with respect to species i, respectively. The reactions were assumed to follow first-order kinetics in terms of bicarbonate, protons, and CO_2, and electrokinetic parameters are given in Table 1.[27,33] We note that different reaction orders (0.1−1), with respect to bicarbonate, have been reported, depending on the electrolyte concentration and applied potential.[33,34] The overpotential (η_m) is given by the difference between the electric potential of DM (ϕ_s) and solution (ϕ_l),

$$\eta_m = (\phi_s - \phi_l) - (E_m^o - 0.059 \times \text{pH}) \tag{21}$$

where E_m^o is the standard potential for reaction m vs SHE. Formation of hydrogen or CO from different proton sources, e.g., H^+ and HCO_3^-, are not differentiable in the thermodynamically relevant scale, i.e., RHE.[32] However, the pK_a of the proton donor is known to affect the kinetics of the reaction. Therefore, we assumed the exchange current densities and onset potentials of electrode reactions are dependent on the pK_a of the proton donor and kinetic parameters were calculated accordingly for reactions in which bicarbonate is the proton donor (see details in the Supporting Information).

Liquid Phase Transport. The material balance of specie i in the electrolyte at the steady state is given by

$$\nabla \cdot N_i = \varepsilon_l \sum_i R_{B,i} + \sum_i R_{i.m} + R_j \tag{22}$$

where $R_{B,i}$ is the source/sink term for homogeneous reactions involving species i. $R_{i,m}$ is the source/sink term of species i for charge transfer reaction m. R_j is the source/sink term for phase transfer reactions. The charge transfer reactions contribute to the source terms in the electrolyte phase for CO_2, OH^-, HCO_3^-, H_2CO_3, and CO_3^{2-} and in the gas phase for CO and H_2 via the equation

$$R_{i,m} = -\sum_m \frac{\upsilon_{i,m} \alpha_v i_m}{n_m F} \tag{23}$$

where n_m is the number of electrons transferred for reaction m and α_v is the specific surface area of the CL. The existence of a gaseous phase at high currents due to gas product formation was assumed to not influence the active surface area and a thin layer of wetting electrolyte was assumed to exist on the surface at the steady state. The gaseous products H_2 and CO were assumed to have negligible solubility and escape directly to the gaseous phase, which was composed of CO_2, CO, and H_2. The rate of phase transfer of CO_2 from the liquid to the gas phase computed using a phase transfer term when $c_{CO_2} > c_{CO_2}^s$,

$$R_j = k_{mt}(c_{CO_2} - c_{CO_2}^s) \tag{24}$$

where k_{mt} is the mass-transfer coefficient, c_{CO_2} is the concentration of CO_2 in the aqueous electrolyte, and $c_{CO_2}^s$ is the solubility of CO_2, which is corrected for the ionic strength by using the experimental data from the literature.[35]

The flux of the specie i (N_i) inside the electrolyte is expressed by the Nernst−Plank equation,

$$N_i = -D_i^{eff} \nabla c_i - z_i \left(\frac{D_i^{eff}}{RT} \right) F c_i \nabla \phi_l + c_i u_l \tag{25}$$

where D_i^{eff}, c_i, and z_i are effective diffusion coefficient, concentration, and charge of the dissolved species in the electrolyte, respectively. ϕ_l and u_l is the potential of the electrolyte and velocity of the solvent, respectively. D_i^{eff} was corrected for porosity (ε_l) and tortuosity (τ_l) by using the Bruggeman relationship,

$$D_i^{eff} = D_i \left(\frac{\varepsilon_l}{\tau_l} \right) \tag{26}$$

where $\tau_l = \varepsilon_l^{-1/2}$ and ε_l is the fraction of the pores filled by liquid calculated via $\varepsilon_l = \varepsilon_m S_l$ where ε_m is the dry porosity of the medium and S_l is the liquid volume fraction. ε_m can be related to solid fraction ε_m^s of the porous medium via $\varepsilon_m^s = 1 - \varepsilon_m$. The electroneutrality condition provides an additional equation to solve for concentration gradients and the electrolyte potential,

$$\sum_{i=1}^{n} z_i c_i = 0 \tag{27}$$

The net current density in the electrolyte (i_l) can be written by the summation of ionic fluxes,

$$i_l = F \sum_{i=1}^{n} z_i j_i \tag{28}$$

where j_i is the combination of diffusion and migration terms in eq 25. The charge conservation equation in the porous electrolyte can be written as

$$\nabla \cdot i_l = \varepsilon_l F \sum_{i=1}^{n} z_i R_{B,i} + \alpha_v \sum_m i_m \tag{29}$$

i_l is related to charge conservation equation in the solid electrode phase via $\nabla \cdot i_l = -\nabla \cdot i_s$, where i_s is the current

https://doi.org/10.1021/acs.iecr.2c00352
Ind. Eng. Chem. Res. 2022, 61, 10461−10473

density in the solid phase. Ohm's law governs the i_s and potential ϕ_s via

$$i_s = \sigma_s^{\text{eff}} \nabla \phi_s \tag{30}$$

where σ_s^{eff} denotes the effective conductivity and ϕ_s is the electronic potential of the solid phase. The conductivity (σ_s) of the medium was corrected with the Bruggeman relationship:

$$\sigma_s^{\text{eff}} = \sigma_s\left(\frac{\varepsilon_m}{\tau_m}\right) \tag{31}$$

The flow of two immiscible phases, e.g., liquid and gas, in porous media were modeled using two-phase Darcy's law, along with the mass conservation for each phase to calculate the convective velocity and gaseous and liquid fractions in the porous electrode.[36] The conservation equations for the liquid and gas at the steady state are

$$\nabla\cdot(\rho_l u_l) = \sum_i R_{i.m} M_i \tag{32}$$

$$\nabla\cdot(\rho_g u_g) = \sum_i R_{i.m} M_i + R_j M_j \tag{33}$$

where ρ_l and ρ_g are the density and u_l and u_g are the velocity of the liquid and gas phases, respectively. The source terms for the gas arise from the phase transfer of CO_2 and electrochemical formation of CO and H_2. The changes in the density of the liquid phase were assumed to be negligible. The velocities of each phase were calculated from an extended form of Darcy's law where the permeability of the medium for each phase was corrected by an additional relative permeability term for the effect of reduced volume due to the presence of the other phase, via

$$u_l = \kappa_m\left(\frac{\kappa_l^{\text{rel}}}{\mu_1}\right)\nabla p_1 \tag{34}$$

$$u_g = \kappa_m\left(\frac{\kappa_g^{\text{rel}}}{\mu_g}\right)\nabla p_g \tag{35}$$

where κ_m is the permeability of the porous medium, and κ_l^{rel} and κ_g^{rel} are relative permeability for liquid and gas phase, respectively. Wylie's model based on a Leverett function, Brooks and Corey, and van Genuchten are the most commonly used semiempirical models used in fuel cell and water electrolysis research.[37] The relative permeabilities of liquid and gas as a function of saturation were computed by the van Genuchten model and can be expressed, respectively, as follows:

$$\kappa_l^{\text{rel}} = \overline{S}_l^{I_{vg}}[1 - (1 - \overline{S}_l^{1/m_{vg}})^{m_{vg}}]^2 \tag{36}$$

$$\kappa_g^{\text{rel}} = \overline{S}_g^{I_{vg}}(1 - (1 - \overline{S}_g)^{1/m_{vg}})^{2m_{vg}} \tag{37}$$

where $\overline{S}_l$ and $\overline{S}_g$ effective phase saturations for liquid and gas, respectively, and I_{vg} and m_{vg} are van Genuchten fit parameters. $\overline{S}_l$ and $\overline{S}_g$ are given by

$$\overline{S}_l = \frac{S_l - S_{rl}}{1 - S_{rl} - S_{rg}} \tag{38}$$

$$\overline{S}_g = \frac{S_g - S_{rg}}{1 - S_{rl} - S_{rg}} \tag{39}$$

where S_{lg} and S_{rg} are the residual liquid and gas saturation, respectively. The volume constraint for the phase saturations can be used to reduce the number of dependent variables,

$$\sum_{i=1}^{n} S_i = S_l + S_g = 1 \tag{40}$$

Additional reduction of dependent variables can be done by relating the liquid and gas phase pressures via the capillary pressure (p_c),

$$p_g = p_l + p_c \tag{41}$$

The constitutive relationship between p_c and liquid saturation in the van Genuchten model is expressed by

$$p_c = p_{\text{ec}}\left(\frac{1}{S_l^{1/m_{vg}}} - 1\right)^{1-m_{vg}} \tag{42}$$

where p_{ec} is the entry capillary pressure that is required to displace water from the largest pore. p_{ec} and m_{vg} were estimated by fitting the experimental pressure−saturation curve of a Toray-090 paper (see Figure S1 in the Supporting Information). Experimental studies in bicarbonate flow cells suggested that only slight differences between the performance of the silver electrodes were reported when carbon papers were treated with PTFE.[18] In addition, electrocapillary effect is considered to increase the wettability at high potentials, even if the starting material is hydrophobic.[38] Therefore, the DM and CL was treated as hydrophilic, and water was assumed to be the wetting phase in all potentials.

Transport of Gases. The transport of gas in the porous medium was assumed to be driven by capillary pressure and diffusion. The flux of the gas-phase molecules (N_k) can be written as a combination of diffusive term (J_k) and a convective term

$$N_k = J_k + \rho_g u_g \tag{43}$$

where ρ_g is the density of the mixture approximated by ideal gas law and u_g is the velocity of the gas phase. The mass conservation equation is given by

$$\nabla\cdot J_k + \nabla\cdot(\rho_g \omega_k u_g) = \sum_i R_{i,m} M_i + R_j \tag{44}$$

where ω_k is the mass fraction of species k. The multicomponent diffusion in the DM was approximated by a mixture-averaged diffusion model. The mixture-averaged diffusion model assumes Fickian-type approximation, wherein the J_k is driven by a gradient in the mass fraction (ω_k) of an individual gaseous species k,

$$J_k = -\left(\rho_g D_k^{\text{eff}} \nabla \omega_k + \rho_g D_k^{\text{eff}} \omega_k \frac{\nabla M_n}{M_n}\right) \tag{45}$$

where D_k^{eff} is the effective diffusion coefficient of species k and M_n is the average molar mass of the mixture. Diffusion coefficients were corrected for porosity and tortuosity by using the Bruggeman relationship,

https://doi.org/10.1021/acs.iecr.2c00352
Ind. Eng. Chem. Res. 2022, 61, 10461−10473

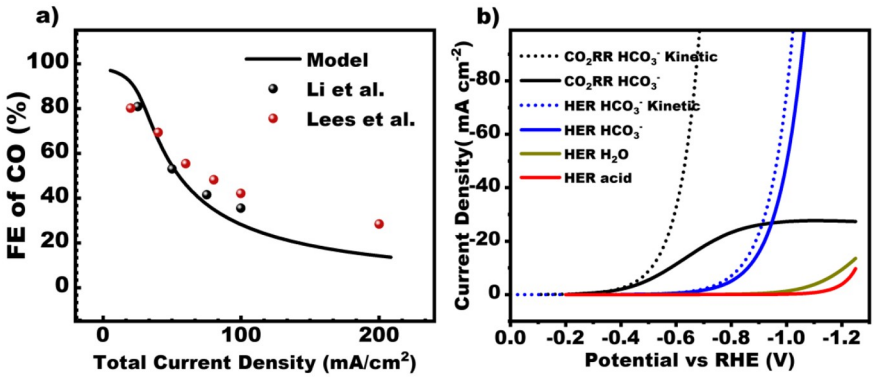

Figure 2. (a) Modeled FE of CO, as a function of total current density, compared to the experimental data reported by Li et al.[5] and Lees et al.[18] Current density in the model represents cathodic current densities. (b) Partial current density versus potential plots for electrochemical CO_2 reduction reaction (CO2RR) and HER evolution with different proton donors. The dashed lines denote when the reaction rate is controlled by kinetics alone without any mass-transfer limitation.

$$D_k^{\text{eff}} = D_k^M\left(\frac{\varepsilon_g}{\tau_g}\right) \tag{46}$$

where $\tau_g = \varepsilon_g^{-1/2}$ and ε_g is the fraction of the pores filled by liquid,

$$\varepsilon_g = \varepsilon_m S_g \tag{47}$$

and the Stefan−Maxwell diffusivity (D_k^M) is given by

$$D_k^M = \frac{1-\omega_k}{\sum_{i\neq k}\frac{x_i}{D_{ki}}} \tag{48}$$

where x_i is the mass fraction.

Boundary Conditions. At the flow channel/DM interface, the concentrations of the aqueous species were set to bulk concentrations, $c_i = c_0$, for a N_2/Ar-purged 3 M $KHCO_3$ solution at 1 atm of pressure. The concentration of CO_2 is assumed to be 0.001 M at the flow channel/DM interface, which is dependent on the intensity of gas purging. The fraction of the gas bubbles was assumed to be low due to the fast-flowing electrolyte in the flow channel and was set to S_l = 0.01 at the flow channel/DM interface, which was equal to the residual saturation of gas phase in the DM.[37] The mole fraction of the gaseous species is highly unpredictable and variant at the DM−flow channel boundary; therefore, we used a Neumann boundary condition where the normal component of the concentration gradient was assumed to be steady through the boundary:

$$-n\cdot\rho_g D_k^M \nabla w_k = 0 \tag{49}$$

while the no flux condition, $-n\cdot J_k = 0$, was specified for gaseous species at the CL/membrane interface.

The electric potential of the solid phase (ϕ_s) was varied between −0.1 V and −2.0 V vs RHE at the flow channel/DM interface. The protons were assumed to be the only charge carrying specie in the membrane and the flux (N_i) at the DM-IEM interface was set via

$$n\cdot N_i = \frac{n\cdot i_l}{z_i F} \tag{50}$$

The flux of all other dissolved and gaseous species, as well as the two existing phases, i.e., gas and liquid, were set to zero at the CL/membrane interface.

Numerical Method. The partial differential equations were discretized by the finite element method and the nonlinear set of equations representing the system were solved iteratively by using Newton's method with a relative tolerance of 0.001. At a given Newton iteration, linear system of equations was solved by COMSOL 5.4, using MUMPS solver. The maximum element size in the mesh was 1 μm in the DM, which was refined down to 0.1 μm at the DM/CL interface, while the maximum element size was 0.01 μm in the CL, which was refined down to 0.3 nm at the CL/IEM interface. The complete mesh consisted of 600 elements, and the model was found insensitive to further refinement of the mesh. The finer meshes at the CL/IEM interface were required not only for resolving sharp concentration gradients, but also homogeneous reactions confined to a small volume next to the membrane.

RESULTS AND DISCUSSION

Using the described transport model that encompassed the system configuration and the homogeneous and electrochemical reactions, we were able to predict the FE of CO in a bicarbonate electrolysis, as a function of current density. The predicted FE is compared with previously reported experimental results in bicarbonate flow cells in Figure 2a.[5,18] Here, we see that the initially high FE of CO (>90%) in the system declines to 30% as current density increases to 100 mA cm^{-2}. The model was quantitative enough for the relative magnitudes of what was recorded in the experiments and very well captured the typical decay of the FE, as a function current density. The reason for such a decay in FE is more evident from Figure 2b, which shows the partial current density of CO and H_2 from different proton donors, as a function of potential. The dashed lines represent the dependence of current density on potential in a 3 M $KHCO_3$ solution when the processes are controlled by the kinetics of the reaction only. Although the CO production rates are much higher than the hydrogen on silver electrodes under kinetically controlled systems, the mass transport effects on the partial current density of CO_2 reduction are apparent in almost all potentials. The partial current density of CO reaches almost a plateau as the HER takes off at higher potentials, which leads to a decline in the FE of CO. This trend was recorded regardless of the type of porous medium and electrolyte in the experimental studies, although the peak CO current density varies with the diffusion medium used.[7] The comparative modeling trend in CO FE

https://doi.org/10.1021/acs.iecr.2c00352
Ind. Eng. Chem. Res. 2022, 61, 10461−10473

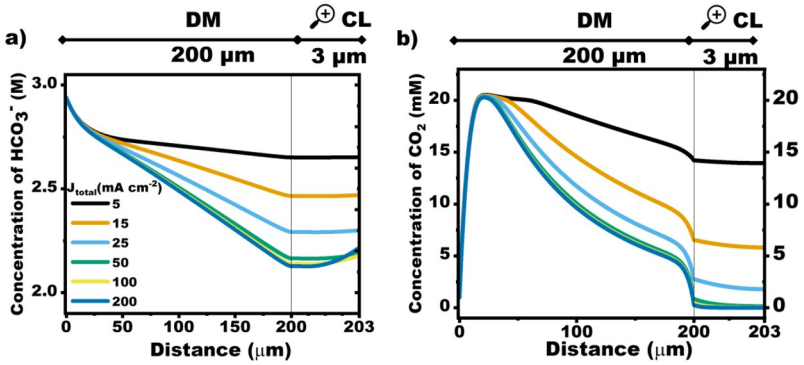

Figure 3. (a) Modeled concentration of HCO_3^- in the porous DM and CL for various current densities; the *x*-axis in the CL has been magnified for convenience. (b) $CO_{2(aq)}$ concentration in the porous DM and CL for various current densities. *x*-axis was magnified in the CL. Current densities represent cathodic current densities.

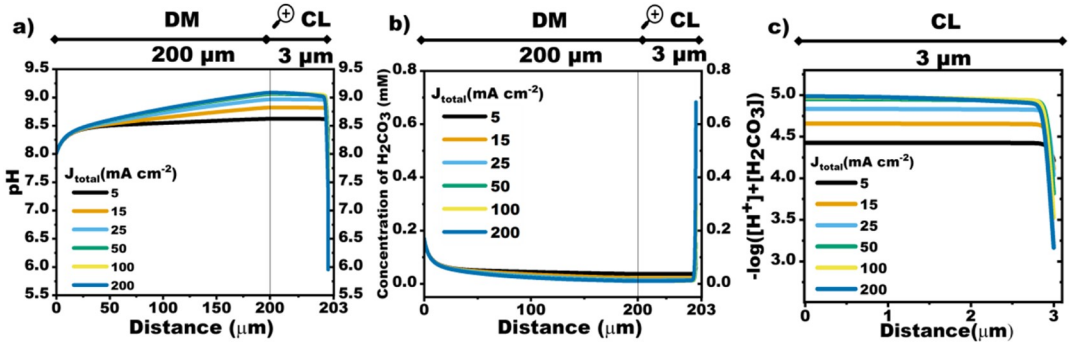

Figure 4. (a) Modeled pH profiles in the DM and CL for various current densities at the steady state; the *x*-axis in the CL has been magnified for the sake of convenience. (b) Steady-state concentration of H_2CO_3 in the DM and CL for various current densities. (c) $p(H^+ + H_2CO_3)$ in the CL, as a function of current density. Current densities represent cathodic current densities.

and partial current density then follows the experimental observations. The contribution of HER from the other proton donors, i.e., H^+ and H_2O, becomes more significant at lower electrolyte concentrations, as discussed later.

The discrepancies between the experiments and model at high current densities are attributed to the assumptions and simplifications made in the model. For instance, the rates of electrochemical CO_2 reduction and HER, and the order of the reaction with respect to bicarbonate and CO_2 might be dependent on electrode preparation, electrolyte concentration, and applied potential.[31,34] In addition, the rates of electrochemical reactions from different proton donors, HCO_3^-, and H^+, are not well-studied, since the charge-transfer kinetics are intertwined. Moreover, product analysis techniques have relatively larger errors associated with them in contrast to the systems where the electrochemical responses can be directly used to measure activity, e.g., water electrolysis and fuel cells. There is currently little information available on the concentration gradients inside the porous medium in bicarbonate flow cells; therefore, the model can provide insight into existing results and serves as a starting point for designing experiments and novel reactors.

As bicarbonate from the flow channel is the primary carbon source for the formed CO, it is essential to understand how the bicarbonate concentration varies throughout the system in order to determine what is limiting CO production. The steady-state concentration of the HCO_3^- in the DM and CL, as a function of current density, is given in Figure 3a, where the *x*-axis has been magnified in the CL for convenience. A concentration gradient is formed along the DM with increasing current density as HCO_3^- is consumed by both electrochemical and homogeneous reactions. However, concentration gradients in the DM and CL reach almost stable values above 50 mA/cm^2 with a slight increase next to the membrane. We note that this prediction is contrary to electrochemical cells using a catholyte between the membrane and the CL in which bicarbonate was predicted to be consumed almost completely at high current density in the porous electrode (>50 mA cm^{-2}).[26,27,58] Therefore, this model suggests that the concentration of the bicarbonate does not reach a limiting value, both as a proton donor and CO_2 source, in the catalytically active regions of the bicarbonate flow cell. Since significant losses in electrocatalytic selectivity toward CO occur well below 100 mA cm^{-2} (Figure 3a), the decrease in HCO_3^- concentrations may not be the primary reason for the decline in FE, as a function of current density.

Figure 3b presents the CO_2 concentration in the porous DM and CL, as a function of current density, where the *x*-axis scale is magnified in the CL for convenience. The CO_2 concentration exhibits a maximum around the solubility limit in 3 M $KHCO_3$ (~21 mM) in the DM and concentration gradients exist both toward CL and flow channel. The gradients become more apparent with increasing current density as more CO_2 is consumed and concentration of CO_2 approaches almost zero in the CL at current densities above 25 mA cm^{-2}. These results suggest that the CO_2-mediated bicarbonate reduction rates are limited by mass transfer and/or the formation of CO_2 at high current densities, even though

https://doi.org/10.1021/acs.iecr.2c00352
Ind. Eng. Chem. Res. 2022, 61, 10461−10473

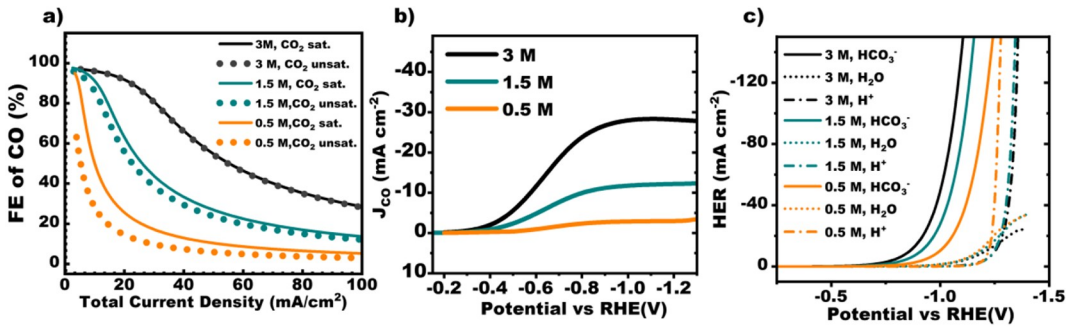

Figure 5. (a) Modeled FE of CO, as a function cathodic current density for different bicarbonate concentrations that are saturated or unsaturated with CO_2. (b) Partial current density of CO for different electrolyte concentrations. Lines represent the sum of HCO_3^- and H_2O as proton donors. (c) Partial current density of H_2 from different proton donors, as a function potential for different electrolyte concentrations. H^+ represents the sum of H_3O^+ and H_2CO_3.

appreciable amounts of dissolved and gaseous CO_2 exist in the DM and escapes to the flow channel (Figure S2 in the Supporting Information). This is consistent with the experiments in bicarbonate cells where CO_2 was detected in the outlet gas stream, which varies with the utilization rate of CO_2 in the catalyst layer.[5,18] Noticeably, the trends in CO_2 concentration and bicarbonate exhibit a similar pattern, as a function of current density. However, CO_2 is almost entirely limited by the formation and/or transport in the CL while substantial amounts of bicarbonate exist at high current densities, which implies that the formation of CO_2 from bicarbonate might be limited by other factors.

Bicarbonate ions not only supply CO_2 to the flow cell by reacting with protons conducted via the membrane but also simultaneously act as a buffer to neutralize the protons and sustain the pH in the CL. Therefore, the consumption of HCO_3^- can influence CO_2 production, electrochemical reaction rates, and the local pH in the CL. The change in the pH for various current densities is given in Figure 4a. The pH in the CL declines adjacent to the membrane as more protons were supplied with increasing current density, while a slightly alkaline pH was predicted in a large fraction of the CL, which extends into the inert DM. It is important to note that the production of CO_3^{2-} and OH^- is spatially distributed in the CL, while the flux of the protons is confined to the CL-membrane interface. This unusual pH gradient implies that there is a competition between the protons supplied from the membrane and electrochemically produced OH^- and CO_3^{2-}. Therefore, the plateau in the CO partial current density (Figure 2b) is a result of the formation of alkaline species (CO_3^{2-} and OH^-) from the electrochemical reactions, which consume the protons required for in situ CO_2 generation. Formation of CO_2 reaches a limit at reasonably high concentrations of bicarbonate (Figure 3a); therefore, unlike the CO formation, the concentration overpotentials were low for H_2 formation from bicarbonate as a proton donor in a broad range of potentials. Therefore, this model suggests that the decrease in the FE of CO in bicarbonate cells at high current densities is a result of limited in situ generation of CO_2 due to the consumption of acidic species in the CL by the alkaline electrochemical products. The feed solution contains primarily HCO_3^-, which requires a single proton to produce a CO_2 molecule (see reactions 1 and 2). On the other hand, each CO_3^{2-} molecule that is formed from electrochemical reactions (reactions 11 and 15) requires two protons for the generation of a CO_2 molecule. Since the concentration of hydroxide is relatively lower (10^{-4}–10^{-5} M) in the CL compared to the carbonate (0.5–1M) at high current densities, the protons conducted through membrane mostly neutralized by the CO_3^{2-}(reaction 3). The reaction between the hydroxide and protons might become significant at higher pH when the solution contains mostly CO_3^{2-}. However, the clash of the acidic and alkaline species in such short distances lead to a relatively lower alkaline pH in the majority of the CL, when compared to the steady-state hydroxide concentrations (>10^{-2} M) at similar current densities in flow cells with AEM and/or flowing catholyte.[25,58]

The concentration of the carbonic acid in the porous DM and CL is given in Figure 4b for various current densities where the *x*-axis in the CL is magnified. There is an apparent increase at the steady-state concentration of the carbonic acid as a function of current density next to the membrane with increasing current density. The concentration gradient of carbonic acid exhibits a profile that is determined by the concentration of protons and bicarbonate, since reaction 1 can be regarded as instantaneous. Because of the protons supply from the membrane and the relatively lower pH adjacent to membrane, significant amounts of carbonic acid exist (0.1–1 mM) at steady state during current flow. The concentration of carbonic acid is usually neglected in modeling and experimental studies, since it is typically <1% of the total carbon content in equilibrium.[29] Reactions 1 and 2 are commonly combined as

$$H^+ + HCO_3^- \underset{k_{11}^b}{\overset{k_{11}^f}{\rightleftharpoons}} CO_2 + H_2O \tag{51}$$

However, the results in this study suggest that the hydration of CO_2 and dehydration of carbonic acid (reaction 2) may not be in equilibrium in the CL under very high proton flux. Therefore, significant amounts of carbonic acid might exist in the CL, even though the formation rate of CO is limited by the generation and transport of CO_2. Similar results were found both experimentally and theoretically in an alkaline medium for the reaction between hydroxide and CO_2 (reaction 5), which has relatively slower kinetics, compared to buffer reactions, and may not be in equilibrium near the electrode surface at high current densities.[59,60] We note that it is reasonable to neglect carbonic acid in models where (local) pH values are >7, since reaction 4 dominantly occurs.

To simplify the source of protons in the model, here we defined a term called total acidic proton content as $-\log(H^+ + H_2CO_3)$ which is analogous to the pH, since carbonic acid can

https://doi.org/10.1021/acs.iecr.2c00352
Ind. Eng. Chem. Res. 2022, 61, 10461–10473

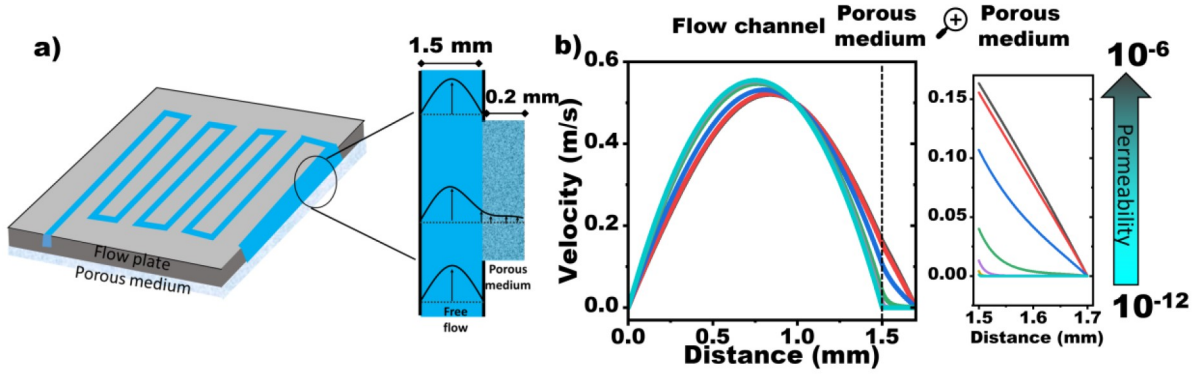

Figure 6. (a) Schematic representation of the pressure-driven free flow in the flow channel (20 mm × 1.5 mm) next to a porous medium (10 mm × 0.2 mm). (b) Calculated velocity profile in the free flow channel and porous medium for 3 M $KHCO_3$ solution with no electrochemical or chemical reactions. Inlet flow rate = 50 mL min^{-1}.

act as a proton source for electrochemical reactions, which was assumed to produce only H_2 on the electrode (see reactions 17 and 18). The $p(H^+ + H_2CO_3)$ of the solution in the CL was plotted as a function of current density in Figure 4c. The $p(H^+ + H_2CO_3)$ exhibited a substantial decrease with increasing current density down to a reasonably acidic value of 3 at 200 mA cm^{-2}. We note that the trends in the $p(H^+ + H_2CO_3)$ adjacent to the membrane, as a function of current density, was remarkably similar, albeit in the opposite direction, to the change of local pH, as a function of current density in conventional electrochemical cells and gas diffusion electrodes with a flowing catholyte.[58] Although the lower pH adjacent to the membrane locally favors hydrogen evolution from acidic species (Figure S3 in the Supporting Information), it does not contribute significantly to the overall FE (<2%) at current densities between 1 and 200 mA cm^{-2}. However, the lower $p(H + H_2CO_3)$ next to the membrane and the resultant changes in the local current density of electrochemical reactions might significantly influence the overall selectivity of the process at low electrolyte concentrations.

In Figure 5a, FE of CO is given as a function of current density in different electrolyte concentrations that are saturated and unsaturated with CO_2. Remarkably, the FE of CO in 3 M bicarbonate is very similar in CO_2 saturated and unsaturated solutions, while there is an apparent difference in the low electrolyte concentrations. These trends are in good agreement with experiments performed in CO_2 and N_2 saturated solutions in bicarbonate flow cells.[5] Even though the solubility of CO_2 is higher in low electrolyte concentrations, the amount of in-situ-generated CO_2 is lower (Figure S4 in the Supporting Information). Therefore, the mass transport of CO_2 from the flow channel significantly contributes to the FE at low concentrations when the solution is saturated with CO_2 (Figure S5 in the Supporting Information). Slower generation of CO_2 is also the primary reason for the decrease in the FE in low electrolyte concentrations, regardless of whether the solution is saturated or not. In Figures 5b and 5c, the partial current density of the CO and HER from different proton donors are shown as a function of electrolyte concentrations that are not saturated with CO_2. The dramatic decrease in the partial current density of CO is the main reason for the decrease of FE in low electrolyte concentrations, even though it is partially compensated by the decline in the rates of HER from bicarbonate as a proton donor. Remarkably, the rate of HER from acidic species, i.e., H_3O^+, H_2CO_3, and water in 0.5 M $KHCO_3$ becomes significant as the CL/membrane interface becomes more acidic, and less bicarbonate is available at the same potential. At 200 mA cm^{-2}, $p(H^+ + H_2CO_3)$ at the CL/membrane interface is ~2.5 in 0.5 M $KHCO_3$ and significant amounts of hydrogen is locally formed next to the membrane (Figure S6 in the Supporting Information), which constitutes 15%−20% of the overall hydrogen produced above 100 mA cm^{-2}(Figure S7 in the Supporting Information). Therefore, we believe that HER is favored over CO_2 reduction next to the cation exchange membranes at high current densities when the concentration of the buffered electrolyte is low or a solid electrolyte with little or no buffering capacity is used. The loss of selectivity is a common observation for gas-fed MEA type of cells using a Nafion or BPM with a cation exchange layer facing the cathode.[21,61,62]

The concentration gradients along the flow cell, unlike the through-plane of the porous electrode, are expected to be much lower, since the single-pass conversion of bicarbonate is typically low, which results from both the high bicarbonate concentration in the feed solution and high flow rates used in the reported experiments.[5,18] Therefore, 1-D models, in the through-plane of the electrodes, are considered to provide a reasonable approximation for the concentration gradients. However, the velocity field from the flow channel might influence convection inside the porous medium, which is schematically depicted in Figure 6a for a pressure-driven flow. When a free-flowing fluid passes adjacent to a porous medium, the fluid attains a certain slip velocity at the flow channel porous medium interface, which decays with a characteristic rate in the porous medium. The depth of penetration and decay of the velocity field is known to be strictly dependent on the properties of the porous medium, e.g., porosity and permeability.[63] The velocity profiles of the 3 M $KHCO_3$ solution inside and next to the porous medium, which were calculated using the Brinkmann and Navier−Stokes equations (see the Supporting Information for details), are given for different permeabilities in Figure 6b. Although the penetration depth and the velocity inside the porous medium with low permeability (<10^{-10} m^2) were small, the influence of free-flow in the flow channel to the convection inside the porous medium is prominent for higher permeability. The permeability of the carbon papers and cloths are in the range of 10^{-10}−10^{-12} m^2 while porous metals have much higher permeability (>10^{-9} m^2).[54,64] We note that, regardless of the porosity and permeability of the porous medium, electrolyte at

https://doi.org/10.1021/acs.iecr.2c00352
Ind. Eng. Chem. Res. 2022, 61, 10461−10473

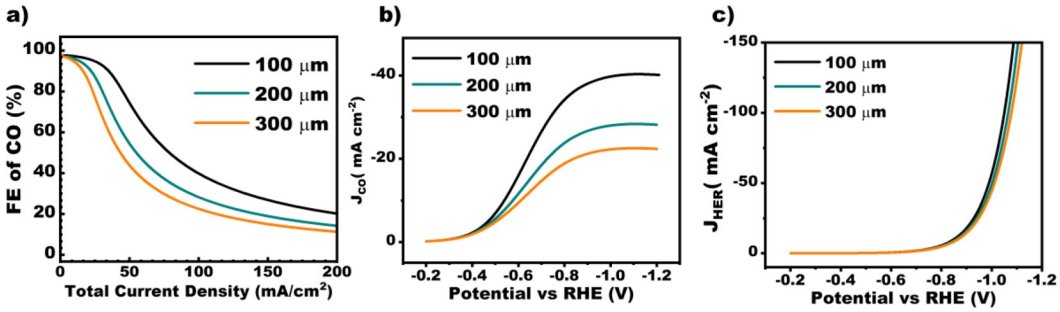

Figure 7. (a) Modeled FE of CO, as a function of the total current density for different DM (i.e., boundary layer, thickness). Current densities represent cathodic current densities. Partial current density of (b) CO and (c) HER with varying DM thickness.

the flow channel-porous medium interface is replenished very quickly; therefore, the local conditions are expected to be substantially different from the CL/membrane interface. In addition, HER is expected to dominate the overall process at the flow channel/porous medium interface if the porous medium is catalytically active and the feed solution does not contain any CO_2.

Coupling electrochemical and homogeneous reactions, multiphase-flow, and momentum transfer in the porous medium next to a free flow can be considerably complex and computationally expensive. In addition, the perpendicular component (along-the-channel) of the velocity is much larger than the through-plane direction (Figure S8 in the Supporting Information). Therefore, the thickness of the diffusion medium was varied to account for the convective velocity from the flow channel, which is similar to changing the boundary layer thickness in mass-transport models in conventional electrochemical cells.[24,65] This can be understood as a quick replenishment of the electrolyte within the penetration depth of the velocity field in the porous medium. Figure 7a presents the change in the FE as a function of the partial current density of CO for different thicknesses of the DM in a 3 M $KHCO_3$ solution. The apparent enhancement of the FE for CO with decreasing DM thickness is a result of a substantial increase in the partial current density of CO (Figure 7b). The mass-transfer-limited current density of CO is almost doubled when the thickness of the DM is reduced from 300 μm to 100 μm. The increase in the CO partial current density is attributed to the faster removal of CO_3^{2-} and OH^-, which can neutralize the protons conducted from the membrane. In contrast to CO_2 electroreduction rates, the change in HER rates is relatively small, as shown in Figure 7c, which is due to substantial amounts of bicarbonate existing in the catalyst layer and concentration overpotentials due to bicarbonate consumption are not significant (Figure 3a). These results suggest that there is room for improving the partial current density and FE of CO by improving the mass transfer inside the porous medium. This was reflected in a recent study where porous metal electrodes, without an inert diffusion medium, were utilized for bicarbonate reduction.[7] The porous metal electrodes have higher permeability, compared to carbon papers, which may allow higher convective flow inside the porous medium, as well as a more electrochemically active surface area.

CONCLUSIONS

A mass transport model was developed to quantify the local concentration of species inside a porous electrode during CO_2-mediated electrochemical bicarbonate reduction to CO. The model captured the experimental trends very well and was quantitative enough to predict the relative magnitudes of current density and FE across a wide range of potential. This model suggests that more CO_2 is generated inside the porous electrode with increasing current density; however, the CO_2 is reduced as fast as it is generated, which leads to very small steady-state CO_2 concentrations in the CL (<1% solubility limit). Since the in-situ production of CO_2 from bicarbonate is proportional to the current density, the CO partial current density increases until the catalyst layer becomes sufficiently alkaline to balance the protons supplied from the membrane. Therefore, concentration overpotentials and the decline in the utilization of protons for CO_2 generation at high current densities leads to a decline in FE of CO. In addition, the model suggests that remarkable amounts of H_2CO_3, as an intermediate in the formation of CO_2, might exist next to the membrane, which favors HER and lowers the FE of bicarbonate electrolysis, especially at low electrolyte concentrations. Moreover, significant concentration overpotentials exist due to the low steady-state concentration of CO_2 in the CL, which can be substantially increased by improving the mass transport and increasing bicarbonate concentration. We believe that mass-transport studies will be particularly important to understand the unconventional CO_2 supply in bicarbonate cells and design novel reactors to improve in-situ generation and the transport of CO_2.

ASSOCIATED CONTENT

Supporting Information

The Supporting Information is available free of charge at https://pubs.acs.org/doi/10.1021/acs.iecr.2c00352.

Description and mathematical details of the 2-D velocity field model, pressure−saturation curve of the DM, gaseous and liquid phase volume fractions as a function current density, concentration gradient of CO_2 in the porous electrode as a function of electrolyte concentration, and local current density of H_2 and CO in the CL (PDF)

AUTHOR INFORMATION

Corresponding Author

Wilson A. Smith − *National Renewable Energy Laboratory, Golden, Colorado 80401, United States; Renewable and Sustainable Energy Institute (RASEI) and Department of Chemical and Biological Engineering, University of Colorado Boulder, Boulder, Colorado 80303, United States; Materials for Energy Conversion and Storage (MECS), Department of*

https://doi.org/10.1021/acs.iecr.2c00352
Ind. Eng. Chem. Res. 2022, 61, 10461−10473

Chemical Engineering, Faculty of Applied Sciences, Delft University of Technology, 2629 HZ Delft, The Netherlands; orcid.org/0000-0001-7757-5281; Email: wilson.smith@colorado.edu

Authors

Recep Kas − *National Renewable Energy Laboratory, Golden, Colorado 80401, United States; Renewable and Sustainable Energy Institute (RASEI), University of Colorado Boulder, Boulder, Colorado 80303, United States;* orcid.org/0000-0003-0508-5894

Kailun Yang − *Materials for Energy Conversion and Storage (MECS), Department of Chemical Engineering, Faculty of Applied Sciences, Delft University of Technology, 2629 HZ Delft, The Netherlands;* orcid.org/0000-0002-3502-1835

Gaurav P. Yewale − *Materials for Energy Conversion and Storage (MECS), Department of Chemical Engineering, Faculty of Applied Sciences, Delft University of Technology, 2629 HZ Delft, The Netherlands*

Allison Crow − *Renewable and Sustainable Energy Institute (RASEI) and Department of Chemical and Biological Engineering, University of Colorado Boulder, Boulder, Colorado 80303, United States*

Thomas Burdyny − *Materials for Energy Conversion and Storage (MECS), Department of Chemical Engineering, Faculty of Applied Sciences, Delft University of Technology, 2629 HZ Delft, The Netherlands;* orcid.org/0000-0001-8057-9558

Complete contact information is available at: https://pubs.acs.org/10.1021/acs.iecr.2c00352

Notes

The authors declare no competing financial interest.

■ ACKNOWLEDGMENTS

This work was authored in part by the National Renewable Energy Laboratory (NREL), operated by Alliance for Sustainable Energy, LLC, for the U.S. Department of Energy (DOE) under Contract No. DE-AC36-08GO28308. This work was supported by the Laboratory Directed Research and Development (LDRD) Program at NREL. The views expressed in the article do not necessarily represent the views of the DOE or the U.S. Government. The U.S. Government retains and the publisher, by accepting the article for publication, acknowledges that the U.S. Government retains a nonexclusive, paid-up, irrevocable, worldwide license to publish or reproduce the published form of this work, or allow others to do so, for U.S. Government purposes.

■ LIST OF SYMBOLS

c_i = concentration of species i (mol m^{-3})
D_i^{eff} = effective diffusion coefficient of species i (m^2 s^{-1})
D_k^M = Stefan−Maxwell diffusion coefficient of the species k (m^2 s^{-1})
E_m^o = standard electrode potential for reaction m (V)
F = Faraday constant (s A mol^{-1})
i_m = partial current density of reaction m (A m^{-2})
$i_{0,m}$ = exchange current density of reaction m (A m^{-2})
i_α = current density in phase α (A m^{-2})
J_k = diffusive mass flux of species k (kg m^{-2} s^{-1})
k_i^{f} = forward rate constant for reaction i
k_i^{b} = backward rate constant for reaction i
k_{mt} = phase transfer rate constant (s^{-1})
M_i = molar mass of the species i (kg mol^{-1})
N_i = total mass flux of species i (kg m^{-2} s^{-1})
p_α = pressure of the phase α (Pa)
p_c = capillary pressure (Pa)
p_{ec} = entry capillary pressure (Pa)
R = gas constant (J K^{-1} mol^{-1})
R_i = source term for process i (mol m^{-3} s)
S_α = volume fraction of phase α
T = temperature (K)
u_α = velocity of the phase α (m s^{-1})
ω_k = weight fraction of specie k
M_n = average molar mass of the gaseous mixture (kg mol^{-1})
M_k = molar mass of the gaseous species k (kg mol^{-1})
α_m = transfer coefficient of reaction m
a_v = specific surface area (m^{-1})
ε_m = porosity of medium m
ε_m^s = solid volume fraction of porous medium m
κ_m = permeability of medium m (m^2)
$\kappa_\alpha^{\text{rel}}$ = effective permeability of phase α
η_m = overpotential for reaction m (V)
ϕ_α = potential of a phase α (V)
σ_m^{eff} = effective conductivity of medium m (S m^{-1})
ρ_m = density of medium m (kg m^{-3})
τ_m = tortuosity of the medium
υ_i = stoichiometric coefficient for species i
μ_i = viscosity of the medium i
δ_i = order of the reaction with respect to specie i

■ REFERENCES

(1) Nitopi, S.; Bertheussen, E.; Scott, S. B.; Liu, X.; Engstfeld, A. K.; Horch, S.; Seger, B.; Stephens, I. E.; Chan, K.; Hahn, C.; et al. Progress and Perspectives of Electrochemical CO_2 Reduction on Copper in Aqueous Electrolyte. *Chem. Rev.* **2019**, *119* (12), 7610−7672.

(2) He, J.; Janaky, C. Recent Advances in Solar-Driven Carbon Dioxide Conversion: Expectations versus Reality. *ACS Energy Lett.* **2020**, *5* (6), 1996−2014.

(3) Kondratenko, E. V.; Mul, G.; Baltrusaitis, J.; Larrazábal, G. O.; Pérez-Ramírez, J. Status and Perspectives of CO_2 Conversion into Fuels and Chemicals by Catalytic, Photocatalytic and Electrocatalytic Processes. *Energy Environ. Sci.* **2013**, *6* (11), 3112−3135.

(4) Sanz-Pérez, E. S.; Murdock, C. R.; Didas, S. A.; Jones, C. W. Direct Capture of CO_2 from Ambient Air. *Chem. Rev.* **2016**, *116* (19), 11840−11876.

(5) Li, T.; Lees, E. W.; Goldman, M.; Salvatore, D. A.; Weekes, D. M.; Berlinguette, C. P. Electrolytic Conversion of Bicarbonate into CO in a Flow. *Cell. Joule* **2019**, *3* (6), 1487−1497.

(6) Li, Y. C.; Lee, G.; Yuan, T.; Wang, Y.; Nam, D.-H.; Wang, Z.; Garcia de Arquer, F. P.; Lum, Y.; Dinh, C.-T.; Voznyy, O.; Sargent, E. H. CO_2 Electroreduction from Carbonate Electrolyte. *ACS Energy Lett.* **2019**, *4* (6), 1427−1431.

(7) Zhang, Z.; Lees, E. W.; Habibzadeh, F.; Salvatore, D. A.; Ren, S.; Simpson, G. L.; Wheeler, D. G.; Liu, A.; Berlinguette, C. P. Porous Metal Electrodes Enable Efficient Electrolysis of Carbon Capture Solutions. *Energy Environ. Sci.* **2022**, *15* (2), 705−713.

(8) Gomes, J.; Santos, S.; Bordado, J. Choosing Amine-Based Absorbents for CO_2 Capture. *Environ. Technol.* **2015**, *36* (1), 19−25.

(9) Mantripragada, H. C.; Zhai, H.; Rubin, E. S. Boundary Dam or Petra Nova−Which Is a Better Model for CCS Energy Supply? *Int. J. Greenhouse Gas Control* **2019**, *82*, 59−68.

(10) Lee, G.; Li, Y. C.; Kim, J.-Y.; Peng, T.; Nam, D.-H.; Sedighian Rasouli, A.; Li, F.; Luo, M.; Ip, A. H.; Joo, Y.-C.; Sargent, E. H. Electrochemical Upgrade of CO_2 from Amine Capture Solution. *Nat. Energy* **2021**, *6* (1), 46−53.

(11) Pellegrini, G.; Strube, R.; Manfrida, G. Comparative Study of Chemical Absorbents in Postcombustion CO_2 Capture. *Energy* **2010**, *35* (2), 851−857.
(12) Li, H.; Gao, J.; Du, Q.; Shan, J.; Zhang, Y.; Wu, S.; Wang, Z. Direct CO_2 Electroreduction from NH_4HCO_3 Electrolyte to Syngas on Bromine-Modified Ag Catalyst. *Energy* **2021**, *216*, 119250.
(13) Welch, A. J.; Dunn, E.; DuChene, J. S.; Atwater, H. A. Bicarbonate or Carbonate Processes for Coupling Carbon Dioxide Capture and Electrochemical Conversion. *ACS Energy Lett.* **2020**, *5* (3), 940−945.
(14) Hori, Y.; Suzuki, S. Electrolytic Reduction of Bicarbonate Ion at a Mercury Electrode. *J. Electrochem. Soc.* **1983**, *130* (12), 2387.
(15) Kortlever, R.; Tan, K. H.; Kwon, Y.; Koper, M. T. M. Electrochemical Carbon Dioxide and Bicarbonate Reduction on Copper in Weakly Alkaline Media. *J. Solid State Electrochem.* **2013**, *17* (7), 1843−1849.
(16) Min, X.; Kanan, M. W. Pd-Catalyzed Electrohydrogenation of Carbon Dioxide to Formate: High Mass Activity at Low Overpotential and Identification of the Deactivation Pathway. *J. Am. Chem. Soc.* **2015**, *137* (14), 4701−4708.
(17) Gutiérrez-Sánchez, O.; Daems, N.; Offermans, W.; Birdja, Y. Y.; Bulut, M.; Pant, D.; Breugelmans, T. The Inhibition of the Proton Donor Ability of Bicarbonate Promotes the Electrochemical Conversion of CO_2 in Bicarbonate Solutions. *J. CO_2 Util.* **2021**, *48*, 101521.
(18) Lees, E. W.; Goldman, M.; Fink, A. G.; Dvorak, D. J.; Salvatore, D. A.; Zhang, Z.; Loo, N. W.; Berlinguette, C. P. Electrodes Designed for Converting Bicarbonate into CO. *ACS Energy Lett.* **2020**, *5* (7), 2165−2173.
(19) Masel, R. I.; Liu, Z.; Yang, H.; Kaczur, J. J.; Carrillo, D.; Ren, S.; Salvatore, D.; Berlinguette, C. P. An Industrial Perspective on Catalysts for Low-Temperature CO_2 Electrolysis. *Nat. Nanotechnol.* **2021**, *16* (2), 118−128.
(20) Mardle, P.; Cassegrain, S.; Habibzadeh, F.; Shi, Z.; Holdcroft, S. Carbonate Ion Crossover in Zero-Gap, KOH Anolyte CO_2 Electrolysis. *J. Phys. Chem. C* **2021**, *125* (46), 25446−25454.
(21) Yan, Z.; Hitt, J. L.; Zeng, Z.; Hickner, M. A.; Mallouk, T. E. Improving the Efficiency of CO_2 Electrolysis by Using a Bipolar Membrane with a Weak-Acid Cation Exchange Layer. *Nat. Chem.* **2021**, *13* (1), 33−40.
(22) Zhang, Z.; Melo, L.; Jansonius, R. P.; Habibzadeh, F.; Grant, E. R.; Berlinguette, C. P. PH Matters When Reducing CO_2 in an Electrochemical Flow Cell. *ACS Energy Lett.* **2020**, *5* (10), 3101−3107.
(23) Kas, R.; Kortlever, R.; Yılmaz, H.; Koper, M. T.; Mul, G. Manipulating the Hydrocarbon Selectivity of Copper Nanoparticles in CO_2 Electroreduction by Process Conditions. *ChemElectroChem.* **2015**, *2* (3), 354−358.
(24) Burdyny, T.; Graham, P. J.; Pang, Y.; Dinh, C.-T.; Liu, M.; Sargent, E. H.; Sinton, D. Nanomorphology-Enhanced Gas-Evolution Intensifies CO_2 Reduction Electrochemistry. *ACS Sustain. Chem. Eng.* **2017**, *5* (5), 4031−4040.
(25) Weng, L.-C.; Bell, A. T.; Weber, A. Z. Towards Membrane-Electrode Assembly Systems for CO_2 Reduction: A Modeling Study. *Energy Environ. Sci.* **2019**, *12* (6), 1950−1968.
(26) Kas, R.; Star, A. G.; Yang, K.; Van Cleve, T.; Neyerlin, K. C.; Smith, W. A. Along the Channel Gradients Impact on the Spatioactivity of Gas Diffusion Electrodes at High Conversions during CO_2 Electroreduction. *ACS Sustain. Chem. Eng.* **2021**, *9* (3), 1286−1296.
(27) Weng, L.-C.; Bell, A. T.; Weber, A. Z. Modeling Gas-Diffusion Electrodes for CO_2 Reduction. *Phys. Chem. Chem. Phys.* **2018**, *20* (25), 16973−16984.
(28) Blake, J. W.; Padding, J. T.; Haverkort, J. W. Analytical Modelling of CO_2 Reduction in Gas-Diffusion Electrode Catalyst Layers. *Electrochim. Acta* **2021**, *393*, 138987.
(29) Palmer, D. A.; Van Eldik, R. The Chemistry of Metal Carbonato and Carbon Dioxide Complexes. *Chem. Rev.* **1983**, *83* (6), 651−731.
(30) Dunwell, M.; Lu, Q.; Heyes, J. M.; Rosen, J.; Chen, J. G.; Yan, Y.; Jiao, F.; Xu, B. The Central Role of Bicarbonate in the Electrochemical Reduction of Carbon Dioxide on Gold. *J. Am. Chem. Soc.* **2017**, *139* (10), 3774−3783.
(31) Resasco, J.; Lum, Y.; Clark, E.; Zeledon, J. Z.; Bell, A. T. Effects of Anion Identity and Concentration on Electrochemical Reduction of CO_2. *ChemElectroChem.* **2018**, *5* (7), 1064−1072.
(32) Jackson, M. N.; Jung, O.; Lamotte, H. C.; Surendranath, Y. Donor-Dependent Promotion of Interfacial Proton-Coupled Electron Transfer in Aqueous Electrocatalysis. *ACS Catal.* **2019**, *9* (4), 3737−3743.
(33) Dunwell, M.; Luc, W.; Yan, Y.; Jiao, F.; Xu, B. Understanding Surface-Mediated Electrochemical Reactions: CO_2 Reduction and Beyond. *ACS Catal.* **2018**, *8* (9), 8121−8129.
(34) Marcandalli, G.; Goyal, A.; Koper, M. T. Electrolyte Effects on the Faradaic Efficiency of CO_2 Reduction to CO on a Gold Electrode. *ACS Catal.* **2021**, *11* (9), 4936−4945.
(35) Yasunishi, A.; Yoshida, F. Solubility of Carbon Dioxide in Aqueous Electrolyte Solutions. *J. Chem. Eng. Data* **1979**, *24* (1), 11−14.
(36) Chen, Z.; Huan, G.; Ma, Y. *Computational Methods for Multiphase Flows in Porous Media*; SIAM: Philadelphia, PA, 2006.
(37) Gostick, J. T.; Fowler, M. W.; Ioannidis, M. A.; Pritzker, M. D.; Volfkovich, Y. M.; Sakars, A. Capillary Pressure and Hydrophilic Porosity in Gas Diffusion Layers for Polymer Electrolyte Fuel Cells. *J. Power Sources* **2006**, *156* (2), 375−387.
(38) Yang, K.; Kas, R.; Smith, W. A.; Burdyny, T. Role of the Carbon-Based Gas Diffusion Layer on Flooding in a Gas Diffusion Electrode Cell for Electrochemical CO_2 Reduction. *ACS Energy Lett.* **2021**, *6* (1), 33−40.
(39) Lide, D. R. *CRC Handbook of Chemistry and Physics* Vol. *85*; CRC Press: Boca Raton, FL, 2004.
(40) Al-Gousous, J.; Salehi, N.; Amidon, G. E.; Ziff, R. M.; Langguth, P.; Amidon, G. L. Mass Transport Analysis of Bicarbonate Buffer: Effect of the CO_2−H_2CO_3 Hydration−Dehydration Kinetics in the Fluid Boundary Layer and the Apparent Effective p K a Controlling Dissolution of Acids and Bases. *Mol. Pharmaceutics* **2019**, *16* (6), 2626−2635.
(41) Newman, J.; Thomas-Alyea, K. E. *Electrochemical Systems*; John Wiley & Sons: Hoboken, NJ, 2012.
(42) Liu, S.; Tao, H.; Zeng, L.; Liu, Q.; Xu, Z.; Liu, Q.; Luo, J.-L. Shape-Dependent Electrocatalytic Reduction of CO_2 to CO on Triangular Silver Nanoplates. *J. Am. Chem. Soc.* **2017**, *139* (6), 2160−2163.
(43) Petrii, O. A.; Tsirlina, G. A. Electrocatalytic Activity Prediction for Hydrogen Electrode Reaction: Intuition, Art, Science. *Electrochim. Acta* **1994**, *39* (11−12), 1739−1747.
(44) Kemula, W.; Krygowski, T. M. *Encyclopedia of Electrochemistry of Elements*; Marcel Dekker: New York, 1979.
(45) Schulz, K. G.; Riebesell, U.; Rost, B.; Thoms, S.; Zeebe, R. E. Determination of the Rate Constants for the Carbon Dioxide to Bicarbonate Inter-Conversion in pH-Buffered Seawater Systems. *Mar. Chem.* **2006**, *100* (1−2), 53−65.
(46) Millero, F.; Huang, F.; Graham, T.; Pierrot, D. The Dissociation of Carbonic Acid in NaCl Solutions as a Function of Concentration and Temperature. *Geochim. Cosmochim. Acta* **2007**, *71* (1), 46−55.
(47) Kron, I.; Marshall, S. L.; May, P. M.; Hefter, G.; Königsberger, E. The Ionic Product of Water in Highly Concentrated Aqueous Electrolyte Solutions. *Monatsh. ChemieChemical Mon.* **1995**, *126* (8), 819−837.
(48) Tu, C. K.; Silverman, D. N. Kinetics of the Exchange of Oxygen between Carbon Dioxide and Carbonate in Aqueous Solution. *J. Phys. Chem.* **1975**, *79* (16), 1647−1651.
(49) Patmonoaji, A.; Suekane, T. Investigation of CO_2 Dissolution via Mass Transfer inside a Porous Medium. *Adv. Water Resour.* **2017**, *110*, 97−106.
(50) Steinkamp, K.; Schumacher, J. O.; Goldsmith, F.; Ohlberger, M.; Ziegler, C. A Nonisothermal PEM Fuel Cell Model Including

Two Water Transport Mechanisms in the Membrane. *J. Fuel Cell Sci. Technol.* **2008**, *5* (1), 011007.
(51) Gostick, J. T.; Ioannidis, M. A.; Fowler, M. W.; Pritzker, M. D. Direct Measurement of the Capillary Pressure Characteristics of Water−Air−Gas Diffusion Layer Systems for PEM Fuel Cells. *Electrochem. Commun.* **2008**, *10* (10), 1520−1523.
(52) Kostecki, R.; Augustynski, J. Electrochemical Reduction of CO_2 at an Activated Silver Electrode. *Berichte Bunsenges. Für Phys. Chem.* **1994**, *98* (12), 1510−1515.
(53) Kita, H. Periodic Variation of Exchange Current Density of Hydrogen Electrode Reaction with Atomic Number and Reaction Mechanism. *J. Electrochem. Soc.* **1966**, *113* (11), 1095.
(54) Phillips, R. K.; Friess, B. R.; Hicks, A. D.; Bellerive, J.; Hoorfar, M. Ex-Situ Measurement of Properties of Gas Diffusion Layers of PEM Fuel Cells. *Energy Procedia* **2012**, *29*, 486−495.
(55) Reyes, A.; Jansonius, R. P.; Mowbray, B. A.; Cao, Y.; Wheeler, D. G.; Chau, J.; Dvorak, D. J.; Berlinguette, C. P. Managing Hydration at the Cathode Enables Efficient CO_2 Electrolysis at Commercially Relevant Current Densities. *ACS Energy Lett.* **2020**, *5* (5), 1612−1618.
(56) Liley, P. E.; Makita, T.; Tanaka, Y. *Properties of Inorganic and Organic Fluids*; Vol. *1*; Taylor & Francis: New York, 1988.
(57) Ozdemir, O.; Celik, M. S.; Nickolov, Z. S.; Miller, J. D. Water Structure and Its Influence on the Flotation of Carbonate and Bicarbonate Salts. *J. Colloid Interface Sci.* **2007**, *314* (2), 545−551.
(58) Burdyny, T.; Smith, W. A. CO_2 Reduction on Gas-Diffusion Electrodes and Why Catalytic Performance Must Be Assessed at Commercially-Relevant Conditions. *Energy Environ. Sci.* **2019**, *12* (5), 1442−1453.
(59) Dunwell, M.; Yang, X.; Setzler, B. P.; Anibal, J.; Yan, Y.; Xu, B. Examination of Near-Electrode Concentration Gradients and Kinetic Impacts on the Electrochemical Reduction of CO_2 Using Surface-Enhanced Infrared Spectroscopy. *Acs Catal.* **2018**, *8* (5), 3999−4008.
(60) Bohra, D.; Chaudhry, J. H.; Burdyny, T.; Pidko, E. A.; Smith, W. A. Modeling the Electrical Double Layer to Understand the Reaction Environment in a CO_2 Electrocatalytic System. *Energy Environ. Sci.* **2019**, *12* (11), 3380−3389.
(61) Vennekoetter, J.-B.; Sengpiel, R.; Wessling, M. Beyond the Catalyst: How Electrode and Reactor Design Determine the Product Spectrum during Electrochemical CO_2 Reduction. *Chem. Eng. J.* **2019**, *364*, 89−101.
(62) Li, Y. C.; Zhou, D.; Yan, Z.; Gonçalves, R. H.; Salvatore, D. A.; Berlinguette, C. P.; Mallouk, T. E. Electrolysis of CO_2 to Syngas in Bipolar Membrane-Based Electrochemical Cells. *ACS Energy Lett.* **2016**, *1* (6), 1149−1153.
(63) Wu, Z.; Mirbod, P. Experimental Analysis of the Flow near the Boundary of Random Porous Media. *Phys. Fluids* **2018**, *30* (4), 047103.
(64) Yuan, W.; Tang, Y.; Yang, X.; Wan, Z. Porous Metal Materials for Polymer Electrolyte Membrane Fuel Cells−A Review. *Appl. Energy* **2012**, *94*, 309−329.
(65) Kas, R.; Yang, K.; Bohra, D.; Kortlever, R.; Burdyny, T.; Smith, W. A. Electrochemical CO_2 Reduction on Nanostructured Metal Electrodes: Fact or Defect? *Chem. Sci.* **2020**, *11* (7), 1738−1749.

https://doi.org/10.1021/acs.iecr.2c00352
Ind. Eng. Chem. Res. 2022, 61, 10461−10473